

Quantum criticality in a three-dimensional spin system at zero field and pressure

K. Yu. Povarov,^{1,*} A. Mannig,¹ G. Perren,¹ J. S. Möller,¹ E. Wulf,¹ J. Ollivier,² and A. Zheludev¹

¹*Neutron Scattering and Magnetism, Laboratory for Solid State Physics, ETH Zürich, Switzerland*

²*Institut Laue-Langevin, 6 rue Jules Horowitz, 38042 Grenoble, France*

(Dated: September 15, 2018)

We report on the spontaneous appearance of antiferromagnetic order in a model gapped quantum paramagnet $\text{Ni}(\text{Cl}_{1-x}\text{Br}_x)_2 \cdot 4\text{SC}(\text{NH}_2)_2$ induced by a change in bromine concentration x . This transition is qualitatively similar to a $z = 1$ magnetic quantum critical point. However, the observed critical scaling of thermodynamic and magnetic properties has rather unusual critical exponents.

Magnetic insulators with their short-range and easily customizable interactions are ideal models of various types of quantum critical points (QCPs) and phase transitions [1, 2]. A paradigmatic example is the transition between a gapped quantum paramagnet and the semiclassical ordered Néel phase [3]. In practice, such QCPs are typically induced by an external magnetic field [4, 5] or by continuously tuning the Hamiltonian parameters. In real quantum magnetic materials, the latter can sometimes be achieved by applying hydrostatic pressure [6, 7]. These zero field QCPs are rare but of a particular interest [8, 9]. They break a continuous spin rotation symmetry and have a dynamical critical exponent $z = 1$. As a result, their properties are quite distinct from those of the more familiar field induced Bose–Einstein magnon condensation [4] or Ising-type transitions [5, 10]. Unfortunately, the experimental necessity of using bulky pressure cells for reaching the quantum critical points in model magnets precludes many measurements needed to probe critical behavior, universality, and scaling laws.

In the present Rapid Communication we report a three-dimensional XY spin system that is *quantum critical in zero applied field and ambient pressure*. Our target material is the well known spin gap compound $\text{Ni}(\text{Cl}_{1-x}\text{Br}_x)_2 \cdot 4\text{SC}(\text{NH}_2)_2$, which we tune to criticality by varying chemical composition. We show that while the $x = 0$ parent compound is gapped, increasing Br concentration x leads to a decrease and eventual closure of the spin gap, followed by the appearance of magnetic long range order with a gapless linear excitation spectrum. We then focus on the material very close to the critical Br content x_c and study the critical properties and scaling at the apparent QCP.

The parent compound $\text{NiCl}_2 \cdot 4\text{SC}(\text{NH}_2)_2$ has been extensively studied as a prototypical spin gap material, particularly in the context of its field-induced quantum phase transitions [13]. A detailed description of the crystal structure, effective magnetic Hamiltonian, and the role of Br substitution on the Cl site can be found, for example, in our previous work [11]. The magnetism is due to $S = 1$ Ni^{2+} ions arranged on a tetragonal lattice, space group $I4$ and lattice parameters $a = 9.56$ and $c = 8.98$ Å. The key energy scales are the easy-plane single ion anisotropy $D = 0.7$ meV, the Heisenberg nearest

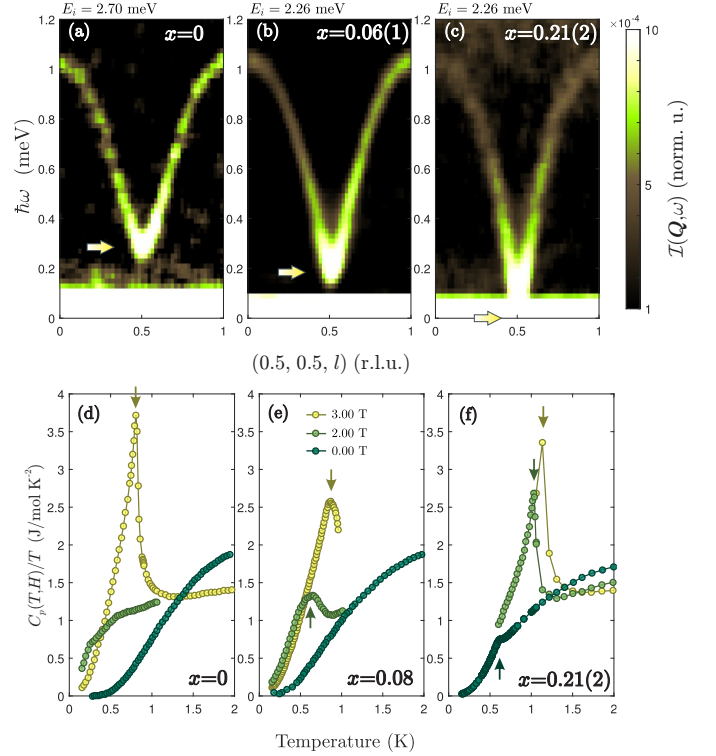


FIG. 1. (a)–(c) Time of flight neutron scattering spectra showing magnetic excitations in $\text{Ni}(\text{Cl}_{1-x}\text{Br}_x)_2 \cdot 4\text{SC}(\text{NH}_2)_2$ with various Br concentration x , traced along $\mathbf{Q} = (0.5, 0.5, l)$ reciprocal space direction. Arrows indicate the corresponding gap values. The data were taken on the IN5 instrument at temperatures of about 100 mK. The incident neutron energy for each data set is indicated separately. The data in (b) are from Ref. [11]. (d)–(f) Specific heat of $\text{Ni}(\text{Cl}_{1-x}\text{Br}_x)_2 \cdot 4\text{SC}(\text{NH}_2)_2$ samples with various x in magnetic field of 0, 2, and 3 T. The arrows show the corresponding ordering temperatures, defined via the specific heat anomalies. The zero-field curve for $x = 0.08$ is reproduced from Ref. [12].

neighbor exchange interactions along the unique tetragonal axis $J_c = 0.15$ meV, and weaker coupling $J_a \simeq 0.1J_c$ within each tetragonal plane. The planar anisotropy term favors a nonmagnetic $S^z = 0$ state for each spin, while interactions favor Néel long range order. In the parent compound the anisotropy term dominates, so that

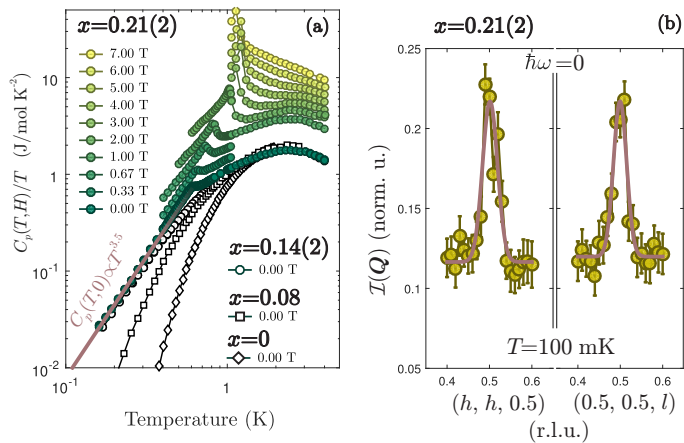


FIG. 2. (a) Specific heat in “overcritical” $x = 0.21(2)$ DTNX sample, given in comparison with zero-field data for “critical” $x = 0.14(2)$, “undercritical” $x = 0.08$, and clean $x = 0$ samples. For nonzero H a vertical offset is introduced for the data: C_p of each curve is multiplied by a factor of 1.3^N , where N enumerates the curves with respect to ascending H . The field is applied along the high symmetry c direction. The zero-field curve for $x = 0.08$ is reproduced from Ref. [12]. (b) The magnetic Bragg peak at $(0.5, 0.5, 0.5)$ r.l.u. in the $x = 0.21(2)$ sample measured at low temperature. Neutron scattering intensity $I(\mathbf{Q})$ for \mathbf{Q} along and transverse to the c direction is shown in the left and right subpanels correspondingly. The points are the experimental data; solid lines are Gaussian fits.

the ground state is a nonmagnetic singlet. The lowest excitations are a highly dispersive $S^z = \pm 1$ doublet with an energy gap $\Delta = 0.3$ meV. These gapped excitations are readily seen by neutron spectroscopy [13]. For reference, in Fig. 1(a) we show our own data. These were taken using two fully deuterated single crystal samples with total mass of 300 mg on the IN5 spectrometer at ILL [14], using a ^3He - ^4He dilution cryostat and neutrons with fixed incident energy of 2.7 meV. The chopper rotation speed for this measurement was set at 12000 rpm. The false color plot shows scattering intensity versus energy transfer $\hbar\omega$ and momentum transfer along $\mathbf{Q} = (0.5, 0.5, l)$ reciprocal space rod, the antiferromagnetic zone center $(0.5, 0.5, 0.5)$ being the global dispersion minimum where the gap is observed directly.

The Br-substituted material $\text{Ni}(\text{Cl}_{1-x}\text{Br}_x)_2 \cdot 4\text{SC}(\text{NH}_2)_2$ has attracted a great deal of interest in the context of effects of disorder on the field-induced quantum phase transitions [12, 15, 16] and magnetic excitations [11, 17]. However, as was clearly shown by neutron spectroscopy studies, the most obvious effect of Br substitution can be understood simply in terms of its influence on *average* exchange and anisotropy constants [11]. Specifically, increasing x decreases the D/J_c ratio and thereby leads to a reduction of the energy gap. For $x = 0.06$ the measured spin excitation spectrum is shown in Fig. 1(b) and

corresponds to $\Delta = 0.2$ meV. Based on a simple linear extrapolation, our previous analysis of the concentration dependence of the gap energy predicted that it will be driven to zero somewhere around $x = 0.2$ [11].

The central result of the present study is that this indeed is the case. Fully deuterated $\text{Ni}(\text{Cl}_{1-x}\text{Br}_x)_2 \cdot 4\text{SC}(\text{NH}_2)_2$ single crystals with $x = 0.21(2)$ were grown from solution following the procedure outlined in Ref. [18]. Single crystal x-ray diffraction carried out on an Apex-II Bruker diffractometer confirmed the structure to be almost identical to that of the parent material, with lattice parameters $a = 9.66$ and $c = 9.08$ Å and a homogeneous Br distribution. Inelastic neutron scattering data for the sample consisting of two coaligned $x = 0.21(2)$ crystals with a total mass of 200 mg was collected on the IN5 spectrometer under the conditions, identical to the experiment of Ref. [11]: temperature of about 100 mK and neutron beam incident energy $E_i = 2.26$ meV (with the choppers rotating at 5000 rpm). The resulting data are shown in Fig. 1(c). In contrast to the other two spectra measured for lower Br content, for $x = 0.21(2)$ the spectrum is gapless and approximately linear in the vicinity of the antiferromagnetic zone center [19].

Not only is the $x = 0.21(2)$ system gapless, it is also magnetically ordered at low temperatures. The magnetic phase transition was detected by specific heat measurements performed on a Quantum Design PPMS with a dilution cryostat insert. To illustrate the ordering evolution with bromine content increase we compare the typical specific heat curves from various samples [clean, $x = 0.08$, and $x = 0.21(2)$] shown in Figs. 1(d)–(f). For an applied magnetic field $H = 3$ T, which exceeds the critical ordering field $H_c^{x=0} = 2.1$ T in the parent compound, all three samples show clear lambda anomalies corresponding to the onset of long-range order. The second field shown, $H = 2$ T, is below $H_c^{x=0}$, but above $H_c^{x=0.08} = 1.1$ T for the $x = 0.08$ sample. Under these conditions, the lambda anomaly is present only in the two sample with higher Br content. Finally, at zero applied field, only the $x = 0.21(2)$ sample still shows a tiny but distinct signature of a phase transition at $T_N \simeq 0.64$ K, while the two other samples remain paramagnetic. The specific heat measurements also confirm the gapless nature of the spectrum in the $x = 0.21(2)$ sample. The log-log specific heat curves shown in Fig. 2(a) contrast the activated (gapped) behavior for $x = 0$ and $x = 0.08$ with a power law (gapless) trend for $x = 0.21(2)$. For later reference, take note of the power law exponent $\alpha = 3.5 \pm 0.05$ fitted in the temperature range 0.15–0.5 K.

Magnetic ordering in the $x = 0.21(2)$ sample is also confirmed by neutron diffraction. In the same IN5 data set as mentioned above, at 100 mK magnetic Bragg peaks are found at $(0.5, 0.5, 0.5)$ reciprocal space positions [symbols in Fig. 2(b)]. These peaks are resolution-limited, as deduced from Gaussian fits to intensity pro-

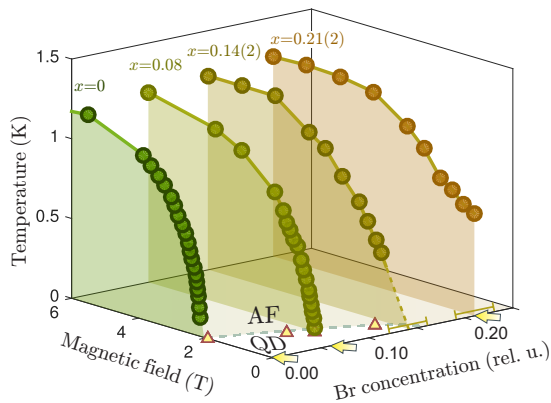


FIG. 3. Phase diagrams of DTNX with various concentration of bromine x in the magnetic field along the c direction. Solid circles are the specific heat data, solid lines are guides to the eye (for $x = 0$ and 0.08 the data is from Refs. [12, 13]). Solid triangles are the $H_c(x)$ values, known from the literature [11–13, 22]. The dashed line marks the *tentative* boundary between the antiferromagnetically ordered (AF) and quantum disordered (QD) states. Concentration errorbars for the present study are also shown. Arrows correspond to the “points” on the phase diagram, at which the neutron data in Fig. 1 was measured.

files measured along different directions (solid lines). An analysis of their intensities [20] (see Supplemental Material for details) allows us to make a crude estimate of the ordered moment $m \simeq 0.3\mu_B$, which is very small compared to the classical saturation value $2\mu_B$ for $S = 1$. Note that in zero applied field the ordering vector in the $x = 0.21(2)$ sample is the same as in the field-induced ordered phase of the $x = 0$ parent compound [21, 22].

The combined phase diagram for $\text{Ni}(\text{Cl}_{1-x}\text{Br}_x)_2 \cdot 4\text{SC}(\text{NH}_2)_2$ based on our data and those found in literature, is shown in Fig. 3. The transition temperatures in this graph were determined from the specific heat anomalies, such as those shown in Figs. 2 and 4. Based on the available data it is not easy to accurately pinpoint the critical concentration x_c at which long range order appears in zero applied field. However, from the known x dependence of the critical field at $T \rightarrow 0$ (triangles in Fig. 3) we can crudely estimate $x_c \simeq 0.16$ [23]. Of all samples synthesized for the present study, the one with the closest Br content has $x = 0.14(2)$. Indeed, this material appears to be on the verge of spontaneous ordering. As shown in Fig. 4, the lambda anomalies in specific heat are unresolved in fields below 0.8 T (or equivalently, temperatures below 300 mK). Nevertheless, down to at least 0.3 T, the heat capacity curves contain precursors of long-range ordering, namely upturns in $C_p(T)/T$ at $T \rightarrow 0$. No such precursors are present in zero applied field. Instead, the specific heat at $H = 0$ seemingly follows the same

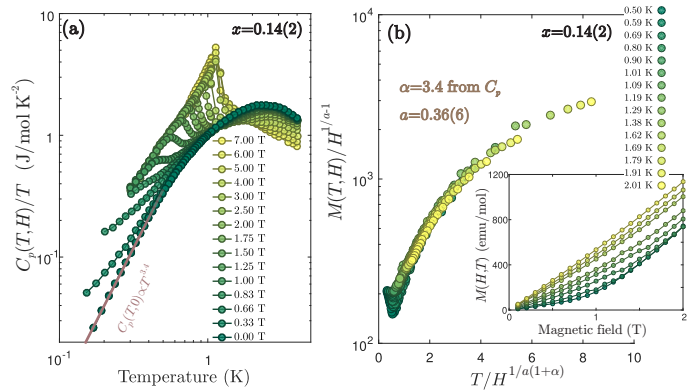


FIG. 4. Thermodynamic properties and scaling in the “critical” $x \simeq 14\%$ DTNX sample. (a) Specific heat in various magnetic fields. At $H = 0$ a low-temperature limit with the specific heat proportional to $T^{3.4}$ is found in the absence of ordering. (b) Main panel: magnetization data plotted in scaled variables. The parameters optimizing the scaling are given in the plot. Inset: original magnetization curves at various temperatures. In all measurements the magnetic field is applied along the high symmetry c direction.

power law

$$C_p(T) \propto T^\alpha \quad (1)$$

with $\alpha = 3.4 \pm 0.15$, within the error coinciding with the value of 3.5 found in a well-ordered $x = 0.21(2)$ sample. In fact, as Fig. 2(a) directly shows, in the low-temperature limit $C_p(T)$ for $x = 0.21(2)$ and $x = 0.14(2)$ samples converge to the same trend. This strongly suggests that for $x = 0.14(2)$ the low-energy excitations are also gapless.

From the experimental point of view, the $x = 0.14(2)$ sample thus appears to be at or very close to a quantum critical point. With this assumption, we can learn more about the underlying physics by checking the scaling of another readily accessible quantity, namely magnetization in the magnetic field, applied along the anisotropy axis (c direction). Usage of the iQuantum ^3He insert for the Quantum Design MPMS SQUID magnetometer allows us to perform the magnetometry measurements in the sub-Kelvin regime. Typical magnetization curves in the $x = 0.14(2)$ sample at different temperatures are shown in the inset of Fig. 4(b). Criticality implies that the free energy of the system obeys the scaling relation [1, 2]:

$$F(T, H) = \lambda^{-1} \mathcal{F}(\lambda^{\frac{1}{1+\alpha}} T, \lambda^a H), \quad (2)$$

for any positive λ , with scaling exponents a and α , the latter being the same as in Eq. (1). For magnetization this gives the following scaling form:

$$M(T, H)/H^{\frac{1-a}{\alpha}} = \mathcal{M}(T/H^{\frac{1}{\alpha(1+\alpha)}}), \quad (3)$$

where $\mathcal{M}(x)$ is an *a priori* unknown scaling function of a single variable. With a proper choice of the exponent a , all measured $M(T, H)/H^{\frac{1-a}{\alpha}}$ data should collapse onto a single curve when plotted vs $T/H^{\frac{1}{\alpha(1+\alpha)}}$. Fixing $\alpha \simeq 3.4$ based on the calorimetric measurements, to find the optimal value of a we minimize the empirical “data overlap” function, as it was done in a number of scaling studies before [10, 24, 25]. With a as the only adjustable parameter, an excellent data collapse [main panel of Fig. 4(b)] is obtained at $a = 0.36(6)$.

If we assume that the transition in $\text{Ni}(\text{Cl}_{1-x}\text{Br}_x)_2 \cdot 4\text{SC}(\text{NH}_2)_2$ can be fully understood in terms of the variation of average Hamiltonian parameters with Br concentration, we are dealing with a $z = 1$ QCP in $d = 3$ dimensions with a spontaneous breaking of $O(2)$ symmetry [26]. Interestingly, the observed critical exponents do *not* agree with this model. There the dynamical exponent $z = 1$, and hyperscaling immediately gives $\alpha = d/z = 3$. There could be a number of trivial explanations for such a discrepancy, such as possibly insufficient dynamic range in our experiments, or an inhomogeneous stress distribution in the samples that is known to have a rather drastic effect on the field induced transition in the parent compound [27]. Another factor may be a violation of hyperscaling due to dangerously irrelevant magnon-magnon interaction [28, 29]. The latter may be of special importance as $z = 1$ $d = 3$ QCP lies exactly at the upper critical dimension of a phase transition that, as in our case, breaks $O(2)$ symmetry. The most interesting interpretation though has to do with disorder, which to this point we deliberately left out of the discussion. The “clean” $O(2)$ transition has the mean-field correlation length critical exponent $\nu = 1/2$ [26] not satisfying the necessary condition $d\nu > 2$ under which the disorder vanishes on large scales. This so-called Harris criterion [30] implies that disorder in $\text{Ni}(\text{Cl}_{1-x}\text{Br}_x)_2 \cdot 4\text{SC}(\text{NH}_2)_2$ is relevant, although whether it has any measurable effect on the criticality of the $z = 2$ field-induced transitions is controversial [27, 31]. In our case, the $z = 1$ transition is expected to be more susceptible. In fact, the QCP is not expected to survive in the presence of disorder, which gives rise to a strongly inhomogeneous weakly ordered Griffiths phase [32]. That disorder must play a role in the concentration-induced transition in $\text{Ni}(\text{Cl}_{1-x}\text{Br}_x)_2 \cdot 4\text{SC}(\text{NH}_2)_2$ is also supported by the unusual specific heat power law in the well ordered $x = 0.21(2)$ sample. Indeed, the contribution of linearly dispersive antiferromagnetic spin waves would simply correspond to $\alpha = 3$.

In any case, further experimental work and theoretical guidance will be required to fully understand the new concentration-induced transition and criticality in $\text{Ni}(\text{Cl}_{1-x}\text{Br}_x)_2 \cdot 4\text{SC}(\text{NH}_2)_2$. Fortunately, the transition occurs in zero applied field and ambient pressure, which

will enable a host of future experiments.

This work was supported by Swiss National Science Foundation, Division II. We would like to thank Dr. S. Gvasaliya (ETH Zürich) for assistance with the sample alignment for the neutron experiment.

* povarovk@phys.ethz.ch

† <http://www.neutron.ethz.ch/>

- [1] S. Sachdev, *Quantum Phase Transitions* (Cambridge University Press, U.K., 2011).
- [2] M. Vojta, “Quantum phase transitions,” Rep. Prog. Phys. **66**, 2069 (2003).
- [3] S. Sachdev, “Quantum criticality: Competing ground states in low dimensions,” Science **288**, 475 (2000); “Quantum magnetism and criticality,” Nat. Physics **4**, 173 (2008).
- [4] T. Giamarchi, C. Rüegg, and O. Tchernyshyov, “Bose-Einstein condensation in magnetic insulators,” Nat. Physics **4**, 198 (2008).
- [5] R. Coldea, D. A. Tennant, E. M. Wheeler, E. Wawrzynska, D. Prabhakaran, M. Telling, K. Habicht, P. Smeibidl, and K. Kiefer, “Quantum Criticality in an Ising Chain: Experimental Evidence for Emergent E8 Symmetry,” Science **327**, 177 (2010).
- [6] Ch. Rüegg, B. Normand, M. Matsumoto, A. Furrer, D. F. McMorrow, K. W. Krämer, H. U. Güdel, S. N. Gvasaliya, H. Mutka, and M. Boehm, “Quantum Magnets under Pressure: Controlling Elementary Excitations in TlCuCl_3 ,” Phys. Rev. Lett. **100**, 205701 (2008).
- [7] M. Thede, A. Mannig, M. Månsson, D. Hüvonen, R. Khasanov, E. Morenzoni, and A. Zheludev, “Pressure-induced quantum critical and multicritical points in a frustrated spin liquid,” Phys. Rev. Lett. **112**, 087204 (2014); G. Perren, J. S. Möller, D. Hüvonen, A. A. Podlesnyak, and A. Zheludev, “Spin dynamics in pressure-induced magnetically ordered phases in $(\text{C}_4\text{H}_{12}\text{N}_2)\text{Cu}_2\text{Cl}_6$,” Phys. Rev. B **92**, 054413 (2015).
- [8] P. Merchant, B. Normand, K. W. Krämer, M. Boehm, D. F. McMorrow, and Ch. Rüegg, “Quantum and classical criticality in a dimerized quantum antiferromagnet,” Nat. Physics **10**, 373 (2008).
- [9] H. D. Scammell and O. P. Sushkov, “Asymptotic freedom in quantum magnets,” Phys. Rev. B **92**, 220401 (2015).
- [10] M. Hälgl, D. Hüvonen, T. Guidi, D. L. Quintero-Castro, M. Boehm, L. P. Regnault, M. Hagiwara, and A. Zheludev, “Finite-temperature scaling of spin correlations in an experimental realization of the one-dimensional Ising quantum critical point,” Phys. Rev. B **92**, 014412 (2015).
- [11] K. Yu. Povarov, E. Wulf, D. Hüvonen, J. Ollivier, A. Paduan-Filho, and A. Zheludev, “Dynamics of a bond-disordered $S = 1$ quantum magnet near $z = 1$ criticality,” Phys. Rev. B **92**, 024429 (2015).
- [12] R. Yu, L. Yin, N. S. Sullivan, J. S. Xia, C. Huan, A. Paduan-Filho, N. F. Oliveira Jr, S. Haas, A. Steppke, C. F. Miclea, F. Weickert, R. Movshovich, E.-D. Mun, B. L. Scott, V. S. Zapf, and T. Roscilde, “Bose glass and Mott glass of quasiparticles in a doped quantum magnet,” Nature **489**, 379 (2012).
- [13] V. S. Zapf, D. Zocco, B. R. Hansen, M. Jaime, N. Harrison, C. D. Batista, M. Kenzelmann, C. Niedermayer,

- A. Lacerda, and A. Paduan-Filho, “Bose-Einstein Condensation of $S = 1$ Nickel Spin Degrees of Freedom in $\text{NiCl}_2\text{-4SC}(\text{NH}_2)_2$,” *Phys. Rev. Lett.* **96**, 077204 (2006); S. A. Zvyagin, J. Wosnitza, C. D. Batista, M. Tsukamoto, N. Kawashima, J. Krzystek, V. S. Zapf, M. Jaime, N. F. Oliveira, and A. Paduan-Filho, “Magnetic Excitations in the Spin-1 Anisotropic Heisenberg Antiferromagnetic Chain System $\text{NiCl}_2\text{-4SC}(\text{NH}_2)_2$,” *Phys. Rev. Lett.* **98**, 047205 (2007); L. Yin, J. S. Xia, V. S. Zapf, N. S. Sullivan, and A. Paduan-Filho, “Direct Measurement of the Bose-Einstein Condensation Universality Class in $\text{NiCl}_2\text{-4SC}(\text{NH}_2)_2$ at Ultralow Temperatures,” *Phys. Rev. Lett.* **101**, 187205 (2008); R. Blinder, M. Dupont, S. Mukhopadhyay, M. S. Grbić, N. Laflorie, S. Capponi, H. Mayaffre, C. Berthier, A. Paduan-Filho, and M. Horvatić, “Nuclear magnetic resonance study of the magnetic-field-induced ordered phase in the $\text{NiCl}_2\text{-4SC}(\text{NH}_2)_2$ compound,” *Phys. Rev. B* **95**, 020404 (2017).
- [14] J. Ollivier and H. Mutka, “IN5 cold neutron time-of-flight spectrometer, prepared to tackle single crystal spectroscopy,” *J. Phys. Soc. Jap.* **80**, SB003 (2011).
- [15] A. Zheludev and T. Roscilde, “Dirty-boson physics with magnetic insulators,” *C. R. Physique* **14**, 740 (2013).
- [16] M. Dupont, S. Capponi, and N. Laflorie, “Disorder-Induced Revival of the Bose-Einstein Condensation in $\text{Ni}(\text{Cl}_{1-x}\text{Br}_x)_2\text{-4SC}(\text{NH}_2)_2$ at High Magnetic Fields,” *Phys. Rev. Lett.* **118**, 067204 (2017).
- [17] A. Orlova, R. Blinder, E. Kermarrec, M. Dupont, N. Laflorie, S. Capponi, H. Mayaffre, C. Berthier, A. Paduan-Filho, and M. Horvatić, “Nuclear Magnetic Resonance Reveals Disordered Level-Crossing Physics in the Bose-Glass Regime of the Br-Doped $\text{Ni}(\text{Cl}_{1-x}\text{Br}_x)_2\text{-4SC}(\text{NH}_2)_2$ Compound at a High Magnetic Field,” *Phys. Rev. Lett.* **118**, 067203 (2017).
- [18] E. Wulf, *Experimental studies on quantum magnets in the presence of disorder* (PhD thesis, ETH Zürich, 2015).
- [19] A detailed analysis of this data will be given elsewhere (Mannig, Povarov *et al.*, in preparation).
- [20] G. L. Squires, *Introduction to the Theory of Thermal Neutron Scattering* (Cambridge University Press, Cambridge, U.K., 2012).
- [21] N. Tsyrlin, C. D. Batista, V. S. Zapf, M. Jaime, B. R. Hansen, C. Niedermayer, K. C. Rule, K. Habicht, K. Prokes, K. Kiefer, E. Ressouche, A. Paduan-Filho, and M. Kenzelmann, “Neutron study of the magnetism in $\text{NiCl}_2\text{-4SC}(\text{NH}_2)_2$,” *J. Phys.: Condens. Matter* **25**, 216008 (2013).
- [22] E. Wulf, D. Hüvonen, J.-W. Kim, A. Paduan-Filho, E. Ressouche, S. Gvasaliya, V. Zapf, and A. Zheludev, “Criticality in a disordered quantum antiferromagnet studied by neutron diffraction,” *Phys. Rev. B* **88**, 174418 (2013).
- [23] The value of $x_c \simeq 0.16$ is also consistent with available microscopic models for DTNX [16]: It corresponds to the percolation threshold of nickel sites, affected by neighboring bromine.
- [24] K. Yu. Povarov, D. Schmidiger, N. Reynolds, R. Bewley, and A. Zheludev, “Scaling of temporal correlations in an attractive Tomonaga-Luttinger spin liquid,” *Phys. Rev. B* **91**, 020406 (2015).
- [25] M. Hälg, D. Hüvonen, N. P. Butch, F. Demmel, and A. Zheludev, “Finite-temperature scaling of spin correlations in a partially magnetized Heisenberg $S = \frac{1}{2}$ chain,” *Phys. Rev. B* **92**, 104416 (2015).
- [26] Z. Zhang, K. Wierschem, I. Yap, Y. Kato, C. D. Batista, and P. Sengupta, “Phase diagram and magnetic excitations of anisotropic spin-one magnets,” *Phys. Rev. B* **87**, 174405 (2013).
- [27] E. Wulf, D. Hüvonen, R. Schönemann, H. Kühne, T. Herrmannsdörfer, I. Glavatsky, S. Gerischer, K. Kiefer, S. Gvasaliya, and A. Zheludev, “Critical exponents and intrinsic broadening of the field-induced transition in $\text{NiCl}_2\text{-4SC}(\text{NH}_2)_2$,” *Phys. Rev. B* **91**, 014406 (2015).
- [28] M. P. A. Fisher, P. B. Weichman, G. Grinstein, and D. S. Fisher, “Boson localization and the superfluid-insulator transition,” *Phys. Rev. B* **40**, 546–570 (1989).
- [29] R. Yu, C. F. Miclea, F. Weickert, R. Movshovich, A. Paduan-Filho, V. S. Zapf, and T. Roscilde, “Quantum critical scaling at a Bose-glass/superfluid transition: Theory and experiment for a model quantum magnet,” *Phys. Rev. B* **86**, 134421 (2012).
- [30] A. B. Harris, “Effect of random defects on the critical behavior of Ising models,” *J. Phys. C: Solid State Phys.* **7**, 1671 (1974).
- [31] Z. Yao, K. P. C. da Costa, M. Kiselev, and N. Prokof’ev, “Critical Exponents of the Superfluid–Bose-Glass Transition in Three Dimensions,” *Phys. Rev. Lett.* **112**, 225301 (2014).
- [32] M. Vojta, “Excitation spectra of disordered dimer magnets near quantum criticality,” *Phys. Rev. Lett.* **111**, 097202 (2013).

SUPPLEMENTAL MATERIAL

Ordered moment estimate

ORDERED MOMENT ESTIMATE

Estimate of the ordered moment was done according to the elastic scattering theory, as given in the textbook by Squires [20]. This analysis is based on the fact that the intensities of lattice Bragg peaks from a given sample on a given instrument can be used to calibrate out the unknown prefactor, relating the measured “arbitrary units” to the absolute units of scattering cross-section. Then, in turn, with this calibration the ordered magnetic moment can be extracted from the magnetic Bragg peak intensities.

As we deal with a time-of-flight dataset, we have to extract the peak intensities in an unconventional manner. The spectrometer has a discrete detector bank, and the sample rotation angles in the experiment are rather discrete too (in comparison to a dedicated diffraction experiment). The discrete structure of the time-of-flight data lacking momentum resolution does not allow one to meaningfully plot the peak in a conventional “rocking curve” manner [20]. Instead one has to work with the voxels of reciprocal space. The intensity within a given voxel is the result of statistical treatment of many events on many detectors, and there is no guarantee that the Bragg condition was precisely matched for a detector

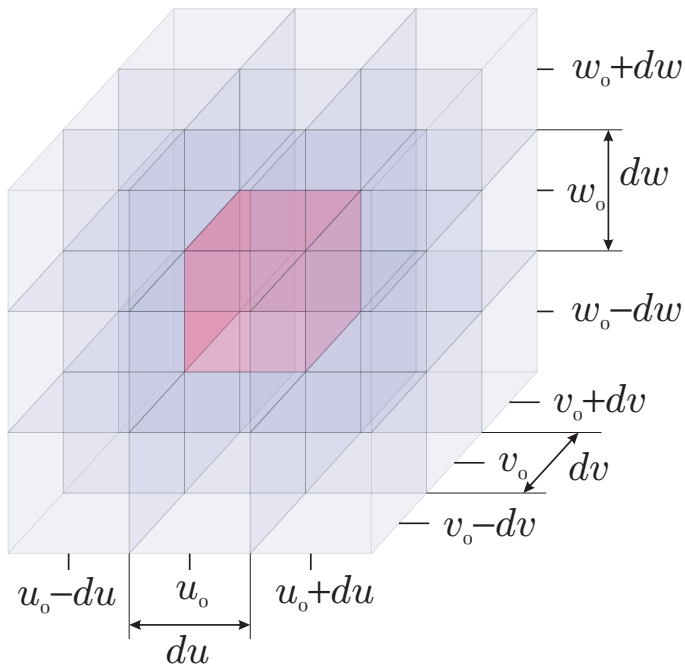


FIG. 5. The Bragg peak intensity determination in the time-of-flight data. The coordinate system of three orthogonal vectors is defined as $\mathbf{u} = (h, h, 0)$, $\mathbf{v} = (0, 0, l)$ and $\mathbf{w} = (-h, h, 0)$. We determine the total intensity in the central “red” block (voxel) of the reciprocal space containing the Bragg peak at (u_0, v_0, w_0) [corresponding to (h_0, h_0, l_0) in the standard r.l.u. notation] and the average of the intensities in the neighboring blocks is taken as the background.

angle and sample rotation angle. As the result of the discreteness, the intensities in the Bragg scattering related voxels may experience some random modulation in the time-of-flight dataset. This makes the analysis below just a *crude estimate* of the ordered magnetic moment.

For the description of the scattering data it is convenient to use the scattering axes basis: $\mathbf{u} = (h, h, 0)$, $\mathbf{v} = (0, 0, l)$ and $\mathbf{w} = (-h, h, 0)$. As the first step we have found the intensities of the peaks. For this we took the following approach (shown in Fig. 5): for each peak we have identified the rectangular block (voxel) of reciprocal space, fully enclosing it. The coordinates of the block center are (u_0, v_0, w_0) and its dimensions are (du, dv, dw) in \mathbf{u} , \mathbf{v} and \mathbf{w} coordinate system. The total intensity (integrated in $\hbar\omega$ from -0.1 to 0.1 meV) in the so defined block is the sum of the peak total intensity and the background. For the background estimate we took the average of intensity in 26 neighboring blocks of the same size, located at $(u_0 \pm du, v_0 \pm dv, w_0 \pm dw)$. After the intensities of the Bragg peaks are obtained, they can be compared to the theory predictions. For the lattice Bragg peaks the intensity is:

$$\mathcal{I}_L(\mathbf{Q}) = I_0 \frac{(2\pi)^3}{V_0} N |\mathcal{F}_L(\mathbf{Q})|^2, \quad (4)$$

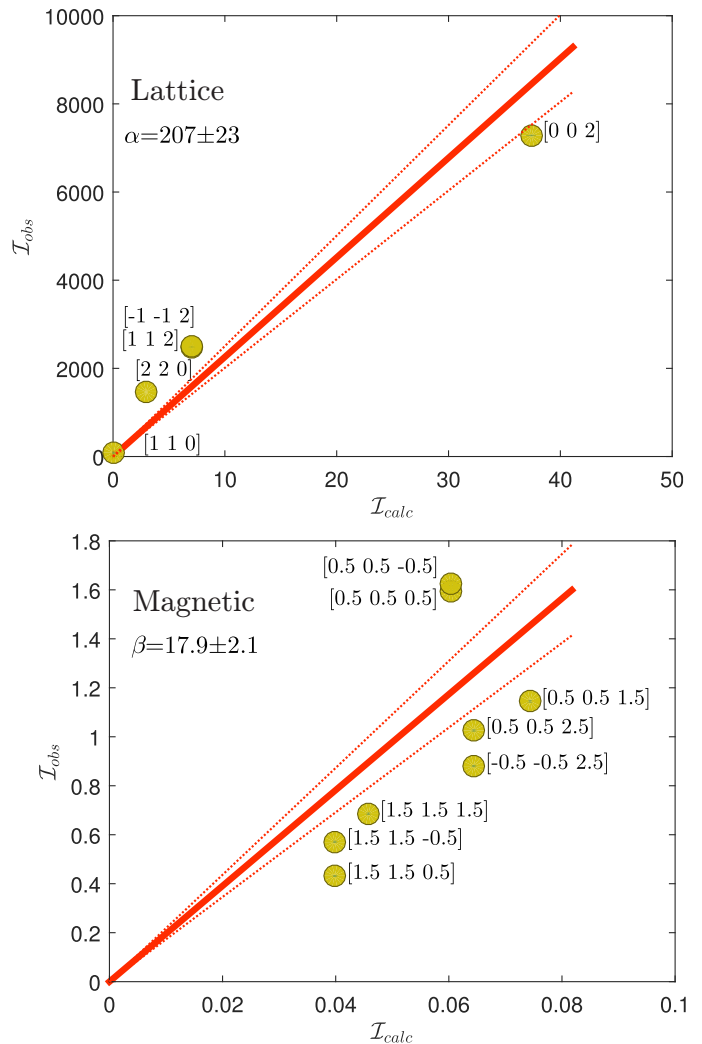


FIG. 6. Observed versus calculated intensities for the lattice (top) and magnetic (bottom) Bragg peaks. Lines show the best linear fit with the tolerance intervals.

where V_0 is the unit cell volume, N is the number of unit cells in the sample, and I_0 is the unknown instrumental coefficient (as no absolute calibration for the scattering intensity was performed). The last term is the lattice cell structure factor:

$$\mathcal{F}_L(\mathbf{Q}) = \sum_{\mathbf{r}_j}^{\text{all c.c.}} b_j e^{i(\mathbf{Q} \cdot \mathbf{r}_j)}. \quad (5)$$

The vectors \mathbf{r}_j are the positions of the atoms within the unit cell and b_j are the corresponding scattering length parameters. The summation goes through all the atoms within the unit cell. The equations (4,5) may be reduced to a simpler form of relation between the observed and calculated intensities $\mathcal{I}_L(\mathbf{Q}) = \alpha \mathcal{I}_L^{\text{calc}}(\mathbf{Q})$, where $\alpha = I_0 (2\pi)^3 N$ is the parameter of interest, which needs to be “calibrated”.

For the magnetic elastic scattering the intensity is:

$$\mathcal{I}_M(\mathbf{Q}) = I_0 \frac{(2\pi)^3 N}{8V_0} (\gamma r_0)^2 |\mathcal{F}_M(\mathbf{Q})|^2 \times \quad (6)$$

$$(1 - (\hat{\mathbf{q}} \cdot \hat{\mathbf{s}})^2) \left(\frac{g}{2}\right)^2 \langle S \rangle^2. \quad (7)$$

Here I_0 , N , and V_0 are the same as in Eq. (4). The magnetic unit cell is 2^3 times bigger than the crystal one, and hence there is a prefactor of 8 appearing twice — for the cell volume and for the number of cells. The prefactor $(\gamma r_0)^2 = 29.06 \text{ fm}^2$ is the universal constant. There is also the magnetic g factor of the Ni^{2+} ion along the ordered moment direction $\hat{\mathbf{s}}$. We assume this direction to be $\hat{\mathbf{s}} = (1, 0, 0)$, and hence $g \simeq 2.3$. The last few terms are the polarization factor (dependent on the angle between $\hat{\mathbf{s}}$ and scattering momentum direction $\hat{\mathbf{q}} = \mathbf{Q}/|Q|$), product of magnetic form-factor and magnetic cell structure factor, and the quantity of our main interest — the ordered moment squared $\langle S \rangle^2$. The product of magnetic form-factor and magnetic cell structure factor, in turn, is expressed as

$$\mathcal{F}_M(\mathbf{Q}) = F(Q) \sum_{\mathbf{r}_j}^{\text{Ni m.c.}} \sigma_j e^{i(\mathbf{Q} \cdot \mathbf{r}_j)}. \quad (8)$$

Like in Eq. (5) there is a summation over the atoms in the unit cell. However, the difference is that now only

the magnetic ions are considered and the summation goes through the magnetic unit cell, which is eight times bigger. There is a factor $\sigma_j = \pm 1$ accounting for the staggered magnetic moment, and $F(Q)$ is the magnetic form factor of the Ni^{2+} ion.

Note, that in Eqs. (5,8) we have neglected the Debye-Waller factors, related to the atomic displacements from the equilibrium positions. At very low temperatures these displacements are small and can be disregarded, as we work with minor momentum transfers.

Again, we can express the relation between the observed and expected intensities as $\mathcal{I}_M(\mathbf{Q}) = \beta \mathcal{I}_M^{\text{calc}}(\mathbf{Q})$, with the prefactor $\beta = I_0 (2\pi)^3 N \langle S \rangle^2$. Then our ordered moment value is expressed as $\langle S \rangle = \sqrt{\beta/\alpha}$ in units of μ_B .

Comparing the observed and calculated intensities (see Fig. 6) we yield $\alpha = 207 \pm 23$ and $\beta = 18 \pm 2$. Hence, $\langle S \rangle = 0.29 \pm 0.03 \mu_B$, which is $15 \pm 2\%$ of the full nickel ion magnetic moment. Again, we would like to reiterate that due to the coarse nature of the dataset the analysis above should be seen only as a crude estimate of $\langle S \rangle$. It also is based on the (very reasonable) assumption that the structure of the ordered phase is identical to the field-induced case analyzed in detail by Tsyrlin *et al.* [21], and in fact does not contain an independent attempt to solve the magnetic structure. Finally, the given error bars are of purely statistical nature and may not reflect a possible systematic error present due to a coarse dataset.